# NASA Technical Memorandum 86280

NASA-TM-86280 19840023490

# AEROTHERMAL LOADS ANALYSIS FOR HIGH SPEED FLOW OVER A QUILTED SURFACE CONFIGURATION



GEORGE C. OLSEN AND ROBERT E. SMITH



AUGUST 1984

NASA
National Aeronautics and
Space Administration

**Langley Research Center**
Hampton, Virginia 23665

# AEROTHERMAL LOADS ANALYSIS FOR HIGH SPEED FLOW OVER A QUILTED SURFACE CONFIGURATION

George C. Olsen
R. E. Smith
NASA Langley Research Center
Hampton, Virginia

## Abstract

Hypersonic laminar flow over a quilted surface configuration was investigated to determine the pressure and heating loads to the surface. The quilted surface configuration simulates an array of metallic Thermal Protection System panels that are bowed in a spherical shape as a result of thermal gradients through the panel thickness. Panel "bowed heights" (deflection of panel from its original flat configuration) from zero to 1.25 times the local boundary layer thickness were investigated for flows both longitudinally and diagonally aligned with the panels. The flow field over the configuration was mathematically modeled using the time-dependant three-dimensional conservation of mass, momentum (Navier-Stokes), and energy equations. A boundary mapping technique was used to obtain a rectangular parallelpiped computational domain, and a MacCormack explicit time-split predictor-corrector finite difference algorithm was used to obtain steady-state solutions. Results show that for bowed heights less than or equal to the local boundary layer thickness total integrated heating loads vary linearly with bowed height. The total integrated heating load on the leading panel and the downstream panels increase to less than 1.44 and 1.26 times the flat plate value, respectively. When the bowed height exceeds the flat plate boundary layer thickness heating rates increase more rapidly, vorticity effects become significant and flow begins to separate ahead of the leading panel.

## Nomenclature

| | |
|---|---|
| $c_v$ | specific heat at constant volume (eq. 5) |
| e | internal energy |
| E | total energy ($e + 1/2\ (u^2+v^2+w^2)$) |
| h | bowed panel height above flat plate |
| K | thermal conductivity of air |
| k | variable grid concentration parameter (eq. A8) |
| $L_\xi, L_\eta, L_\zeta$ | differential operators (eq. B1) |
| p | pressure |
| $R_g$ | gas constant (eq. 4) |
| r | radius measured from panel center |
| $r_o$ | radius of flat-plate/spherical region intersection |
| T | temperature |
| t | time |
| u, v, w | velocity components in x, y, and z directions, respectively |
| $\bar{Y}$ | functional relationship between the physical and computational domains (eqs. A7 and A9) |
| x, y, z | coordinate directions |
| $\delta_{fp}$ | flat plate boundary-layer thickness at $x = x_{cl}$ |
| $\epsilon$ | one-half the fillet width |
| $\xi, \eta, \zeta$ | transformed coordinates |
| $\bar{\eta}$ | redistributed transformed coordinate (eq. A8) |
| $\mu$ | viscosity (eq. 6) |
| $\rho$ | density |
| $\delta_{ij}$ | stress tensor (eq. 2) |

### Subscripts

| | |
|---|---|
| max | maximum coordinate value |
| cn | coordinate value at center of panel n (n = 1, 2, 3) |

## Introduction

Metallic Thermal Protection Systems (TPS) have been proposed as viable concepts for hypersonic vehicles and as an alternative for the current Reusable Surface Insulation (RSI) TPS on the Space Shuttle.[1-4] Metallic TPS would be less fragile than RSI, last longer, eliminate gaps, and offer the advantage of mechanical fastening. Concepts combining thin foils of titanium and/or superalloy materials sometimes combined with metallic honeycomb and/or insulation materials have been fabricated. These concepts are weight competitive with RSI.

However, the use of metallic TPS can introduce some physical phenomena not present in the RSI system. One such phenomenon is thermal bowing of the metallic TPS panels.[3] Bowing occurs because metals have relatively large coefficients of thermal expansion and because in the course of performing their function as a thermal protection system the TPS panels must sustain large temperature gradients through their thickness. These conditions lead to larger thermal expansion of the outer portion of the panel than of the inner portion. The square panels are held down at the corners but otherwise thermal expansion is unrestrained to minimize thermal stresses. As a result the center of the panel bows out into the stream so that the vehicle moldline is altered. An array of panels would take on a lightly quilted configuration.

High speed flow over a thermally bowed metallic TPS introduces complicated three-dimensional flow phenomena that perturb the flow field and significantly alter the wall pressure and heating rate distributions. No analytical studies of a configuration resembling the thermally bowed TPS were found in the literature. A preliminary study of flow over spherical dome protuberences showed that the domes

did significantly effect the flow fields.[5] In some cases separated flow regions developed and trailing vortices formed, significantly altering downstream heating rates.

This study was conducted to determine pressure and heating rate distributions on a quilted surface configuration simulating an array of thermally bowed metallic TPS panels in a high speed laminar flow field. The flow field simulates Mach 7 flight at 120,000 ft. altitude and is similar to the test condition in reference 4. Sections of arrays two and one-half panels in length have been modeled for flows longitudinally and diagonally aligned with the panels. Computer storage limitations restricted the model to 0.31 ft. square panels. Bowed panel heights, h, in the range $0 \leq h \leq 0.25$ inches were considered in a flow field whose flat plate boundary layer height, $\delta_{fp}$, is 0.20 inches.

The analysis employs the same formulation and numerical procedures used in the preliminary study of spherical dome protuberances[5] a three-dimensional formulation of the time dependent equations for conservation of mass, momentum (Navier-Stokes), and energy and a MacCormack explicit time-split predictor-corrector finite difference algorithm. Steady-state solutions were obtained on Langley's Cyber 203 vector processing computer. The results of those solutions are presented in this paper using state-of-the-art computer graphics techniques.

## Analysis

### Governing Equations

Air, the fluid medium, was modeled as a compressible, viscous, thermally conducting gas and was assumed to be an isotropic newtonian ideal gas in local thermodynamic equilibrium. The three-dimensional time-dependent system of equations describing this model include the continuity equation (conservation of mass), the Navier-Stokes equations of motion (conservation of momentum), the energy equation (conservation of energy), and the ideal gas equation (thermodynamic state equation). These equations have been derived in the literature[6] and are shown below written in cartesian tensor form where repeated indices indicate a summation over the range of indices (i.e. $\frac{\partial(\rho w_i)}{\partial x_i}$ for i = 1, 2, 3 is $\left(\frac{\partial(\rho w_1)}{\partial x_1} + \frac{\partial(\rho w_2)}{\partial x_2} + \frac{\partial(\rho w_3)}{\partial x_3}\right)$, where $w_1$, $w_2$, $w_3$ are the velocity components u, v, w, and $x_1$, $x_2$, $x_3$ are the coordinate directions x, y, z. The Kronecker delta, $\delta_{ij}$; equals 1 when i = j and equals zero when $i \neq j$.

Continuity equation,

$$\frac{\partial \rho}{\partial t} + \frac{\partial(\rho w_i)}{\partial x_i} = 0 \qquad (1)$$

Navier-Stokes equations of motion,

$$\frac{\partial(\rho w_i)}{\partial t} + \frac{\partial(\rho w_i w_j)}{\partial x_j} - \frac{\partial(\tau_{ij})}{\partial x_j} = 0$$

where

$$\tau_{ij} = -\delta_{ij} P + \mu\left(\frac{\partial w_i}{\partial x_j} + \frac{\partial w_j}{\partial x_i} - \frac{2}{3}\delta_{ij}\frac{\partial w_k}{\partial x_k}\right) \qquad (2)$$

for i = 1, 2, 3

Energy equation,

$$\frac{\partial(\rho E)}{\partial t} + \frac{\partial(\rho E w_j)}{\partial x_j} - \frac{\partial}{\partial x_j}\left(K\frac{\partial T}{\partial x_j}\right) - \frac{\partial(w_i \tau_{ij})}{\partial x_j} = 0 \qquad (3)$$

Ideal gas state equation,

$$P = \rho R_g T \qquad (4)$$

These equations along with the ideal gas relationship,

$$e = c_v T \qquad (5)$$

and the Sutherland viscosity formula,

$$\mu = 2.270\ \frac{T^{3/2}}{T + 198.6} \times 10^{-8}\ \frac{\text{lb sec}}{\text{ft}^2} \qquad (6)$$

constitute a set of five partial differential equations and one algebraic equation in six dependant variables: three velocity components, u, v, and w; density, $\rho$; temperature, T; and pressure, P.

The physical domain grids and array dimensions for the quilted surface configurations with longitudinally and diagonally aligned flow are shown in figure 1. Points corresponding to corners of the metallic TPS panels were fixed while the remainder of the panels bowed in a spherical manner simulating the thermal expansion that would occur during aerodynamic heating. The resulting surface topography is a lightly quilted pattern. Leading panels were faired into the upstream flat plate by extending the spherical shape. The intersections between the spherical regions and the flat plates were made mathematically smooth by modeling a fillet region at $r_o \pm \epsilon$ with a Hermite polynomial (where $r_o$ = 0.21 ft. and $\epsilon$ = 0.01 ft.). Panel "bowed heights" (deflection of panel from original flat configuration) between $0 \leq h/\delta_{fp} \leq 1.25$ were modeled in 0.25 $h/\delta_{fp}$ increments. The longitudinally aligned flow configuration has a longitudinal symmetry plane at the center of the panels and another at the edge of the panels, reducing the required computational model to one-half the panel width (fig. 1a). The diagonally aligned flow configuration has longitudinal symmetry planes on the panel diagonals, reducing the required computational model to one-half a panel diagonal (fig. 1b). The domains of the longitudinally and diagonally aligned flow configurations were discretized into 94 x 32 x 26 and 76 x 45 x 26 grids, respectively. The resulting computations contained approximately 5 x $10^5$ degrees of freedom.

## Boundary Conditions

A boundary layer profile was input as the upstream boundary plane (x = 0) data and held constant throughout the computations. The boundary layer profile was determined using a two-dimensional boundary layer analysis[7] for flow over a flat plate. The length of flat plate ahead of the three dimensional region was selected to produce a flat plate boundary layer thickness, $\delta_{fp}$ = 0.2 in., at the center of the leading panel (X = 0.31 ft.). The free stream conditions for Mach 7 flight at an altitude of 120,000 ft. used to initiate the calculations are shown in Table I. Using the converged flow field solution for one bowed height as the initial condition for the next greater bowed height reduced the time required for convergence by approximately one-third.

Both side boundaries are planes of symmetry on which the dependent variables are determined by quadratic extrapolation from interior points so that the cross flow gradients, $\partial/\partial z$, of all state variables are zero and the cross flow velocity, w, is zero. The upper boundary and downstream boundaries are specified as no-change boundaries, i.e., set equal to the plane next to them. The wall is a no-slip boundary with a constant temperature of 1440°R. This wall temperature is both the upper use temperature and the flat plate radiation equilibrium temperature for the input boundary conditions for a titanium TPS assuming a high emittance coating and zero thermal diffusivity.

## Computational Domain

In order to generate a boundary fitted coordinate system and provide increased resolution in the boundary layer, the physical domain (fig. 1) was transformed into a rectangular parallelepiped computational domain using a two-boundary grid generation technique.[8] The computational domain has equally spaced grid lines in the $\xi$, $\eta$, and $\zeta$ directions. Transformation of the governing equations to the computational domain is shown in appendix A.

## Numerical Procedure

A finite-difference solution to the governing equations was attained using the second-order accurate MacCormack explicit time-split predictor-corrector algorithm.[9] A fourth-order eddy-viscosity-like damping term was included to promote stability in the regions of large pressure gradients.[10] Both the algorithm and the damping term are further discussed in appendix B.

## Programming and Computer Processing

The numerical procedure has been programmed to run on Langley's Cyber 203 vector processing machine using 32-bit (half word) arithmetic, to provide increased speed and storage. Vector processing and the large data base required an interleaved storage data management system to promote efficient processing. The data management system and vector processing are described in reference 8.

## Results and Discussion

The effects of hypersonic flow over a quilted surface configuration simulating spherically bowed metallic TPS panel arrays with both longitudinally and diagonally aligned flow were analyzed. Bowed heights from zero to 1.25 times the local flat plate boundary layer height were investigated. The results of the analysis are shown herein with the aid of computer graphics displays and vector plots. All similar parameters, pressures, heating rates, and velocity vectors, are displayed on a common scale to facilitate direct comparisons.

## Flow Field Perturbations

The effects of bowed height on the surface and flow field pressure distributions for longitudinally and diagonally aligned flow are shown in figures 2 and 3, respectively. Computer graphics displays (fig. 2a and 3a) present the pressure distributions on the wall, on the two flow field symmetry planes, and on the outflow plane--over 8400 data points in each display. Pressure at the initial plane is 0.1614 psi and pressure variations range from 0.088 psi to 0.395 psi for the $h/\delta_{fp}$ = 1.25 case. Plots of the peak pressure for each panel as a function of bowed height are shown in figures 2b and 3b. The leading panels in both flow configurations generate shock waves and have pressure distributions similar to those found on spherical dome protuberances.[5] The peak pressure on the windward side of the leading panel increases exponentially with increasing bowed height to 2.22 times the flat plate value at $h/\delta_{fp}$ = 1.25.

Downstream panels in longitudinally aligned flow (fig. 2) are shielded by the leading panel and generate much weaker shock waves than the leading panel. The peak pressures on panels two and three increase linearly with bowed height to 1.33 and 1.29 times the flat plate value, respectively, at $h/\delta_{fp}$ = 1.25 (fig. 2b). Expansion regions form on the leeside of each panel resulting in a flow field with alternating high and low pressures which tend to merge away from the surface.

Panel two in diagonally aligned flow (fig. 3) is only partially shielded by the leading panel. Impinging flow generates a shock wave similar to the leading panel but not as strong. The peak pressure on panel two is 1.78 times the flat plate value at $h/\delta_{fp}$ = 1.25 (fig. 3b). Panel three is shielded by the leading panel and generates a much weaker shock wave than the leading panel. The peak pressure on panel three increases linearly to 1.40 times the flat plate value at $h/\delta_{fp}$ = 1.25. Again, the alternating compression and expansion regions produce a flow field with alternating high and low pressure regions, in addition the offset panels cause these regions to be interlaced in the transverse direction.

The effect of surface configuration on the flow near the wall for $h/\delta_{fp}$ = 1.0 is shown by the streamwise/crossflow velocity vectors in figure 4. Vectors for the longitudinally aligned flow (fig. 4a) show moderate three-dimensional flow relief on the windward side of the leading dome but little relief on the leeside or on downstream panels. Separated flow regions have developed ahead of the lead panel and in the interpanel valleys normal to the flow. Vectors for diagonally

aligned flow (fig. 4b) show strong three dimensional flow relief on both the windward and leeside of all panels. The flow follows the diagonal valleys between panels. This interaction of flow field and surface contour generates vortices that impinge on downstream panels. A small separated flow region has developed ahead of the leading panel similar to the spherical dome protuberances in reference 5. In addition, larger separated flow regions have developed in the depressed corner regions of the panels. Much larger separated flow regions develop on the windward side of the leading panels for both flow alignments when $h/\delta_{fp}$ is increased to 1.25.

Wall Heating Rate Distributions

The effects of bowed height on the surface heating rates for longitudinally and diagonally aligned flow are shown in figures 5 and 6, respectively. Computer graphics displays (fig. 5a and 6a) present the heating rate distributions on the walls. The average heating rate on the flat plates is approximately 1.5 Btu/ft$^2$ sec and ranges between 0.12 and 4.88 Btu/ft$^2$-sec for $h/\delta_{fp}$ = 1.25. Plots of the peak heating rate for each panel as a function of bowed height are shown in figures 5b and 6b and plots of the total integrated panel heat loads as a function of bowed height are shown in figures 5c and 6c. Heating rate distributions on the windward side of the leading panel in both flow configurations are similar to those found on spherical dome protuberances.[5] The peak heating rates on the leading panels increase exponentially with bowed height to 3.31 times the flat plate value at $h/\delta_{fp}$ = 1.25.

Heating rate distributions for longitudinally aligned flow (fig. 5a) show increased windward side heating on each panel and decreased heating in the valleys between panels as bowed height increases. A separated flow region in front of the $h/\delta_{fp}$ = 1.25 leading panel slightly perturbs the local heating rate. The heating rate distribution on the $h/\delta_{fp}$ = 1.25 third panel also shows the incipient formation of off-center high heating rate areas caused by impinging vortices from upstream panels. Peak heating rates on panels two and three increase approximately linearly with bowed height to 2.05 and 2.02 times the flat plate value, respectively, at $h/\delta_{fp}$ = 1.25. Panel three shows a slightly non-linear increase between $h/\delta_{fp}$ = 1.0 and 1.25 as a result of increased heating caused by the impinging vortices. Total panel integrated heating loads (fig. 5c) do not increase as sharply as peak heating loads because of reduced leeside heating rates. Panel one heat load increases exponentially with bowed height to 1.61 times the flat plate value at $h/\delta_{fp}$ = 1.25. Panel two heat load increases approximately linearly with bowed height to 1.33 times the flat plate value at $h/\delta_{fp}$ = 1.25.

Heating rate distributions for diagonally aligned flow (fig. 6a) show similar windward side and valley heating trends and separated flow perturbations. However, panel two and three heating rates vary significantly from the longitudinally aligned flow configuration as the bowed height exceeds $h/\delta_{fp}$ = 0.50. Panels two and three have increased heating regions on the centerline of the panels that are the result of flow field impingment. However, impinging vortices also cause regions of higher heating to form off-center that result in exponential increases in peak panel heating (fig. 6b) to 2.60 and 2.34 times the flat plate value, respectively, at $h/\delta_{fp}$ = 1.25. Although peak panel heating rates for diagonally aligned flow are about the same or higher than those for longitudinally aligned flow, total panel integrated heat loads (fig. 6c) are less as a result of lower leeside heating. Total heat loads on panels one and two increase exponentially to 1.54 and 1.21 times the flat plate value, respectively, at $h/\delta_{fp}$ = 1.25.

These computations have been done assuming a constant wall temperature of 1440°R. However, because of the wide range of heating rates encountered, the wall temperature will not be uniform. The equivalent wall radiation equilibrium temperature for the peak heating rate for each panel was computed assuming zero thermal diffusivity of the wall, a constant heat transfer coefficient, and a surface emissivity of 0.72. The resulting peak wall temperatures shown in figure 7 are conservative. The equivalent wall radiation equilibrium temperature for all the panels longitudinally aligned flow (fig. 7a) increase nearly linearly over the range of bowed heights. Panels one, two, and three temperatures increase to 1826, 1603, and 1573°R, respectively, at $h/\delta_{fp}$ = 1.25. The temperatures for the panels diagonally aligned flow (fig. 7b) behave in a similar manner until the vorticity induced heating on the downstream panels causes a non-linear increase in heating. Panels one, two, and three temperatures increase to 1826, 1679, and 1702°R, respectively, at $h/\delta_{fp}$ = 1.25.

These data show that for bowed panels that are submerged in the boundary layer, i.e., $h/\delta_{fp} < 1.0$, vorticity induced heating is negligible and flow does not separate on the windward side of the leading panel. Integrated heat loads on the leading panels and downstream panels increase to less than 1.44 and 1.26 times the flat plate value, respectively. In comparison, under similar flow conditions experimentally measured total heat loads on simulated Shuttle RSI tiles increase an average of 1.27 times the flat plate value as a result of the gaps between tiles.[11] Local radiation equilibrium temperature increased less than 20 percent on leading panels and 11 percent on downstream panels.

True spherical deformation of a metallic TPS panel, as prescribed in this study, would occur only if the heating were uniform. In reality the aerothermal heating analysis is coupled to the TPS panel thermal/structural analysis through the heating rate distribution. The actual thermal deformation will vary from a spherical shape because the heating rate is nonuniform. Solution of a fully coupled problem of this magnitude is beyond current capabilities. An iterative solution between the fluid analysis and the thermal/structural analysis would be expensive.

## Conclusions

An analytical study of high-speed flow over a quilted surface configuration simulating spherically bowed metallic Thermal Protection System panel arrays was conducted to determine the associated flow field and the effect on panel aerothermal heating. Flow longitudinally and diagonally aligned with panels whose bowed heights

varied from 0 to 1.25 times the flat plate boundary layer thickness was investigated. The flow field was modeled as three-dimensional, laminar viscous, and thermally conducting flow utilizing the continuity equations of mass, momentum, and energy. Results show that for bowed heights less than or equal to the flat plate boundary layer thickness integrated heat loads on leading and downstream panels increase to less than 1.44 and 1.26 times the flat plate value, respectively, and radiation equilibrium temperatures increase by less than 280 and 160°R, respectively. These increases are similar to those seen on Reusable Surface Insulation tiles due to gaps. When the bowed height exceeds the flat plate boundary layer thickness heating rates increase rapidly, vorticity effects become significant (especially for diagonally aligned flow), and flow begins to separate ahead of the leading panel.

## References


[1]Kelly, H. N.; Rummler, D. R.; and Jackson, R. L.: Research in Structures and Materials for Future Space Transportation Systems - An Overview. AIAA Paper No. 79-0859, May 1979.

[2]Shideler, J. L.; Kelly, H. N.; Avery, D. E.; Blosser, M. L.; and Adelman, H. M.: Multiwall TPS - An Emerging Concept. Journal of Spacecraft and Rockets, Vol. 19, No. 4, July-August 1982, p.358.

[3]Jackson, R. J.; and Dixon, S. C.: A Design Assessment of Multiwall Metallic Stand-Off and RSI Reusable Thermal Protection System Including Space Shuttle Applications. NASA TM-81780, April 1980.

[4]Shideler, John L.; Webb, Granville L.; and Pittman, Claud M.: Verification Tests of Durable TPS Concepts, AIAA Paper No. 84-1767, June 1984.

[5]Olsen, George C.; and Smith, R. E.: Analysis of Aerothermal Loads on Spherical Dome Protuberances. AIAA Paper No. 83-1557, June 1983.

[6]Schlichting, H.: Boundary Layer Theory, McGraw-Hill, 1968.

[7]Harris, Julius E.; and Blanchard, Doris K.: Computer Program for Solving Laminar, Transitional, or Turbulent Compressible Boundary-Layer Equations for Two-Dimensional and Axisymmetric Flow. NASA TM 83207, 1982.

[8]Smith, R. E.: Two-Boundary Grid Generations for the Solution of the Three-Dimensional Compressible Navier-Stokes Equations, NASA TM-83123, May 1981.

[9]MacCormack, R. W.; and Paullay, A. J.: Computational Efficiency Achieved by Time Splitting of Finite Difference Operations, AIAA Paper No. 72-154, January 1972.

[10]MacCormack, R. W.; and Baldwin, B. S.: A Numerical Method for Solving the Navier-Stokes Equations with Application to Shock Boundary Interactions, AIAA Paper No. 75-1, January 1975.

[11]Avery, Don Earl: Experimental Aerodynamic Heating to Simulated Space Shuttle Tiles in Laminar and Turbulent Boundary Layers with Variable Flow angles. MS Thesis, George Washington University, Nov. 1983.


## Appendix A
## Governing Equations in Computational Domain

Transformation of the governing differential equations, eqs. 1, 2, and 3, to the computational domain requires replacement of all spatial derivatives, $\partial/\partial X_i$ for $i = 1, 2, 3$, with the following,

$$\frac{\partial}{\partial X_i} = \frac{\partial}{\partial C_\ell}\frac{\partial C_\ell}{\partial X_i} \tag{A1}$$

where $C_\ell$ for $\ell = 1, 2, 3$ are the transformed coordinates $\xi$, $\eta$ and $\zeta$, i.e., $\frac{\partial}{\partial X_i} = \frac{\partial}{\partial \xi}\frac{\partial \xi}{\partial X_i} + \frac{\partial}{\partial \eta}\frac{\partial \eta}{\partial X_i} + \frac{\partial}{\partial \zeta}\frac{\partial \zeta}{\partial X_i}$. The resulting equations of motion are,

Continuity,

$$\frac{\partial \rho}{\partial t} + \frac{\partial(\rho w_i)}{\partial C_\ell}\frac{\partial C_\ell}{\partial X_i} = 0 \tag{A2}$$

Navier Stokes equations of motion

$$\frac{\partial(\rho w_i)}{\partial t} + \frac{\partial(\rho w_i w_j)}{\partial C_\ell}\frac{\partial C_\ell}{\partial X_j} - \frac{\partial(\tau_{ij})}{\partial C_\ell}\frac{\partial C_\ell}{\partial X_j} = 0 \tag{A3}$$

where

$$\tau_{ij} = -\delta_{ij} P + \mu\left(\frac{\partial w_i}{\partial C_m}\frac{\partial C_m}{\partial X_j} + \frac{\partial w_j}{\partial C_m}\frac{\partial C_m}{\partial X_i} - \frac{2}{3}\delta_{ij}\frac{\partial w_k}{\partial C_m}\frac{\partial C_m}{\partial X_k}\right)$$

Energy Equation

$$\frac{\partial(\rho E)}{\partial t} + \frac{\partial}{\partial C_\ell}\left(\rho E w_j - K\frac{\partial T}{\partial C_m}\frac{\partial C_m}{\partial X_j}\right)\frac{\partial C_\ell}{\partial X_j} - \frac{\partial(w_i\,\tau_{ij})}{\partial C_\ell}\frac{\partial C_\ell}{\partial X_j} = 0 \tag{A4}$$

Written in short form the system of partial differential equations is,

$$\frac{\partial U}{\partial t} + \frac{\partial F}{\partial C_\ell}\frac{\partial C_\ell}{\partial x} + \frac{\partial G}{\partial C_\ell}\frac{\partial C_\ell}{\partial y} + \frac{\partial H}{\partial C_\ell}\frac{\partial C_\ell}{\partial z} = 0 \tag{A5}$$

where,

$$U = \begin{bmatrix} \rho \\ \rho u \\ \rho v \\ \rho w \\ \rho E \end{bmatrix}$$

$$F = \begin{bmatrix} \rho u \\ \rho uu - \tau_{11} \\ \rho uv - \tau_{12} \\ \rho uw - \tau_{13} \\ \rho Eu - K \frac{\partial T}{\partial C_m} \frac{\partial C_m}{\partial x} - (u\tau_{11} + v\tau_{12} + w\tau_{13}) \end{bmatrix}$$

$$G = \begin{bmatrix} \rho v \\ \rho uv - \tau_{12} \\ \rho vv - \tau_{22} \\ \rho vw - \tau_{32} \\ \rho Ev - K \frac{\partial T}{\partial C_m} \frac{\partial C_m}{\partial y} - (u\tau_{12} + v\tau_{22} + w\tau_{32}) \end{bmatrix}$$

$$H = \begin{bmatrix} \rho w \\ \rho uw - \tau_{13} \\ \rho vw - \tau_{23} \\ \rho ww - \tau_{33} \\ \rho Ew - K \frac{\partial T}{\partial C_m} \frac{\partial C_m}{\partial z} - (u\tau_{13} + v\tau_{23} + w\tau_{33}) \end{bmatrix}$$

The required Jacobian transform matrix,

$$J = \frac{\partial C_l}{\partial X_j} = \begin{bmatrix} \frac{\partial \xi}{\partial x} & \frac{\partial \xi}{\partial y} & \frac{\partial \xi}{\partial z} \\ \frac{\partial \eta}{\partial x} & \frac{\partial \eta}{\partial y} & \frac{\partial \eta}{\partial z} \\ \frac{\partial \zeta}{\partial x} & \frac{\partial \zeta}{\partial y} & \frac{\partial \zeta}{\partial z} \end{bmatrix} \quad (A6)$$

is determined by a linear mapping of the boundaries at $\eta = 0$ and $\eta = 1$ of the computation domain onto the boundaries of the physical domain at $y = 0$ and $y = y_{max}$ in the following form;

$$Y = Y(\xi, 1, \zeta)\,\eta + Y(\xi, 0, \zeta)\,(1 - \eta). \quad (A7)$$

Further transformation to increase resolution in the boundary layer region entails an exponential grid stretching in the $\eta$ direction of the form,

$$\bar{\eta} = \frac{e^{k\eta} - 1}{e^{k} - 1} \quad (A8)$$

where k is a free parameter that adjusts grid spacing. Equation A7 becomes,

$$\bar{Y} = Y(\xi, 1, \zeta)\,\bar{\eta} + Y(\xi, 0, \zeta)\,(1 - \bar{\eta}) \quad (A9)$$

For the geometry of the subject problem the resulting Jacobian matrix is of the form,

$$J = \begin{bmatrix} \frac{1}{x_{max}} & 0 & 0 \\ \frac{\partial \eta}{\partial x} & \frac{\partial \eta}{\partial y} & \frac{\partial \eta}{\partial z} \\ 0 & 0 & \frac{1}{z_{max}} \end{bmatrix} \quad (A10)$$

where $\frac{\partial \eta}{\partial x}$, $\frac{\partial \eta}{\partial y}$, and $\frac{\partial \eta}{\partial z}$, which vary for the flat plate, fillet, and spherical regions of each panel n (n = 1, 2, 3) as defined by the radius measured from the center of each panel

$$r_n = \sqrt{(x_{max}\,\xi - x_{cn})^2 + (z_{max}\,\zeta - z_{cn})^2} \quad (A11)$$

where $x_{cn}$ is the streamwise coordinate and $z_{cn}$ is the spanwise coordinate of each panel center.

These Jacobian elements are calculated and stored for each grid point in the domain thus allowing the solutions from the computational domain to be transformed to the physical domain.

Substituting the transform Jacobian (eq. A10) into the short form of the equation system (eq. A5) reduces the system to the following,

$$\frac{\partial U}{\partial t} + \frac{\partial F}{\partial \xi}\frac{1}{x_{max}} + \frac{\partial F}{\partial \eta}\frac{\partial \eta}{\partial x} + \frac{\partial G}{\partial \eta}\frac{\partial \eta}{\partial y} + \frac{\partial H}{\partial \eta}\frac{\partial \eta}{\partial z} + \frac{\partial H}{\partial \zeta}\frac{1}{z_{max}} = 0 \quad (A12)$$

## Appendix B
## Numerical Procedure

A finite-difference solution to the governing equations was attained using the second-order accurate MacCormack explicit time-split predictor-corrector algorithm.[9] The algorithm splits the differencing scheme into a series of one-dimensional operators. The operator in the principle flow direction, $L_\xi$, advances the computation by one time increment while the operators in the other two coordinate directions, $L_\eta$ and $L_\zeta$, are divided into two steps of one-half a time increment each and applied symmetrically around the principle flow direction operator. This arrangement allows the principle flow direction operator to run at a Courant, Friedricks, Lewy (CFL) number close to the optimum value of one. The operators are applied serially as follows:

$$U^{n+1}_{i,j,k} = \left[L_\eta\left(\frac{\Delta t}{2}\right)\right]\left[L_\zeta\left(\frac{\Delta t}{2}\right)\right]\left[L_\xi(\Delta t)\right]\left[L_\zeta\left(\frac{\Delta t}{2}\right)\right]\left[L_\eta\left(\frac{\Delta t}{2}\right)\right]\left(U^{n}_{i,j,k}\right) \quad (B1)$$

Each operator has two steps, a predictor step that advances the solution by its time increment based on a backward spatial differencing of the one-dimensional equations and a corrector step that recalculates the advancement based on a forward spatial differencing of the predicted results and averages the result with the predictor. The predictor must therefore lag the corrector by a spatial increment in each coordinate direction. The combination of these two steps results in a second-order-accurate differencing scheme in time and space. As an example the first operation $L_\eta(\Delta t/2)$ applied to the data at time step n is as follows:

Predictor step:

$$\bar{U}_{i,j,k} = U^n_{i,j,k} - \frac{\frac{\Delta t}{2}}{\Delta n}\left[\left(F^n_j - F^n_{j-1}\right)\frac{\partial n}{\partial x} + \left(G^n_j - G^n_{j-1}\right)\frac{\partial n}{\partial y} + \left(H^n_j - H^n_{j-1}\right)\frac{\partial n}{\partial z}\right]_{i,k} \quad \text{(B2)}$$

Corrector step:

$$\bar{U}^{*n+1}_{i,j,k} = \frac{1}{2}\left(\bar{U}_{i,j,k} + U^n_{i,j,k} - \frac{\frac{\Delta t}{2}}{\Delta n}\left[\left(\bar{F}_{j+1} - \bar{F}_j\right)\frac{\partial n}{\partial x} + \left(\bar{G}_{j+1} - \bar{G}_j\right)\frac{\partial n}{\partial y} + \left(\bar{H}_{j+1} - \bar{H}_j\right)\frac{\partial n}{\partial z}\right]_{i,k}\right) \quad \text{(B3)}$$

Where bars over the variables indicate predictor values and asterisks over the variables indicate an intermediate result in the serial application of operators as shown in equation B1. The other operators have similar form.

Although a complete stability analysis of this algorithm is not available the CFL limit yields a conservative time step as follows,

$$\Delta t \leq \min\left[\frac{|u|}{\Delta x} + \frac{|v|}{\Delta y} + \frac{|w|}{\Delta z} + c\sqrt{\frac{1}{\Delta x^2} + \frac{1}{\Delta y^2} + \frac{1}{\Delta z^2}}\right]^{-1} \quad \text{(B4)}$$

where c is the local speed of sound.

In the formulation of this algorithm terms of order three and higher have been truncated. These terms are not significant in many flow regimes, but, when modeling high energy flow fields with strong shocks, as in this paper, they can be significant. In the region of a shock, where pressure gradients are extremely sharp, the higher-order terms act as dampers on the pressure disturbance. When these dampers are missing, as in most finite-difference formulations, they can be simulated by adding terms such as the fourth-order eddy-viscosity-like term suggested in reference 10 which has the form

$$\alpha\,\Delta t\,\Delta C_1^3\left(\frac{\partial}{\partial C_\ell}\,\frac{|u| + c}{4P}\left|\frac{\partial^2 P}{\partial C_\ell^2}\right|\right)\frac{\partial U}{\partial C_\ell} \quad \text{(B5)}$$

Implementing this smoothing term required adding a term of the following form to each vector component, both predictor and corrector steps, in the F, G, and H vectors defined in equation A5.

$$\alpha\,\frac{|P_{i+1,j,k} - 2P_{i,j,k} + P_{i-1,j,k}|}{P_{i+1,j,k} + 2P_{i,j,k} + P_{i-1,j,k}}\left(|u_{i,j,k}| + c_{i,j,k}\right)\left(U_{i+1,j,k} - U_{i,j,k}\right) \quad \text{(B6)}$$

where $\alpha$ is a free adjustable parameter whose range is $0 < \alpha < 1/2$, c is the local speed of sound and U is the vector defined in equation A5. The term is of significant magnitude only when the pressure gradient is large.

Table I Specified conditions

| | |
|---|---|
| **Free Stream** | |
| Mach Number, $M_\infty$ | 7 |
| Velocity, $u_\infty$, ft/sec | 7131 |
| Pressure, $P_\infty$, $lb_f/in^2$ | $4.92 \times 10^{-4}$ |
| Temperature, $T_\infty$, R | 432 |
| Density, $\rho_\infty$, $lb_m/ft^3$ | $4.432 \times 10^{-4}$ |
| **Wall** | |
| Temperature, $T_w$, R | 1440 |
| Reynolds Number, $R_e$ | $3.38 \times 10^5$ |

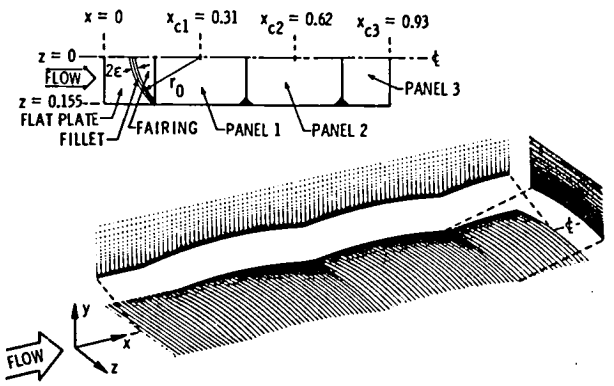


(a) Longitudinal aligned flow

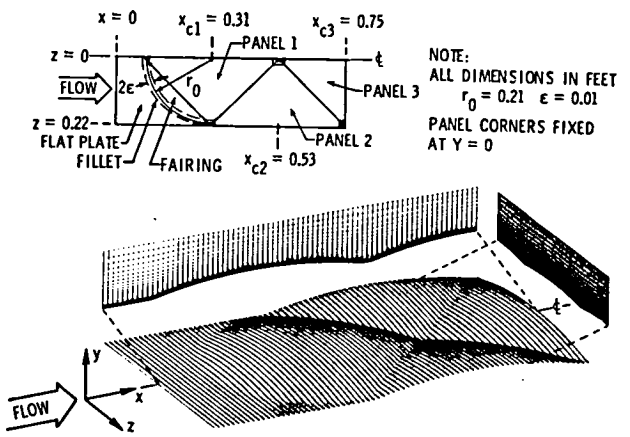


(b) Diagonally aligned flow

Fig. 1 Physical domain grids and array dimensions for quilted surface configurations.

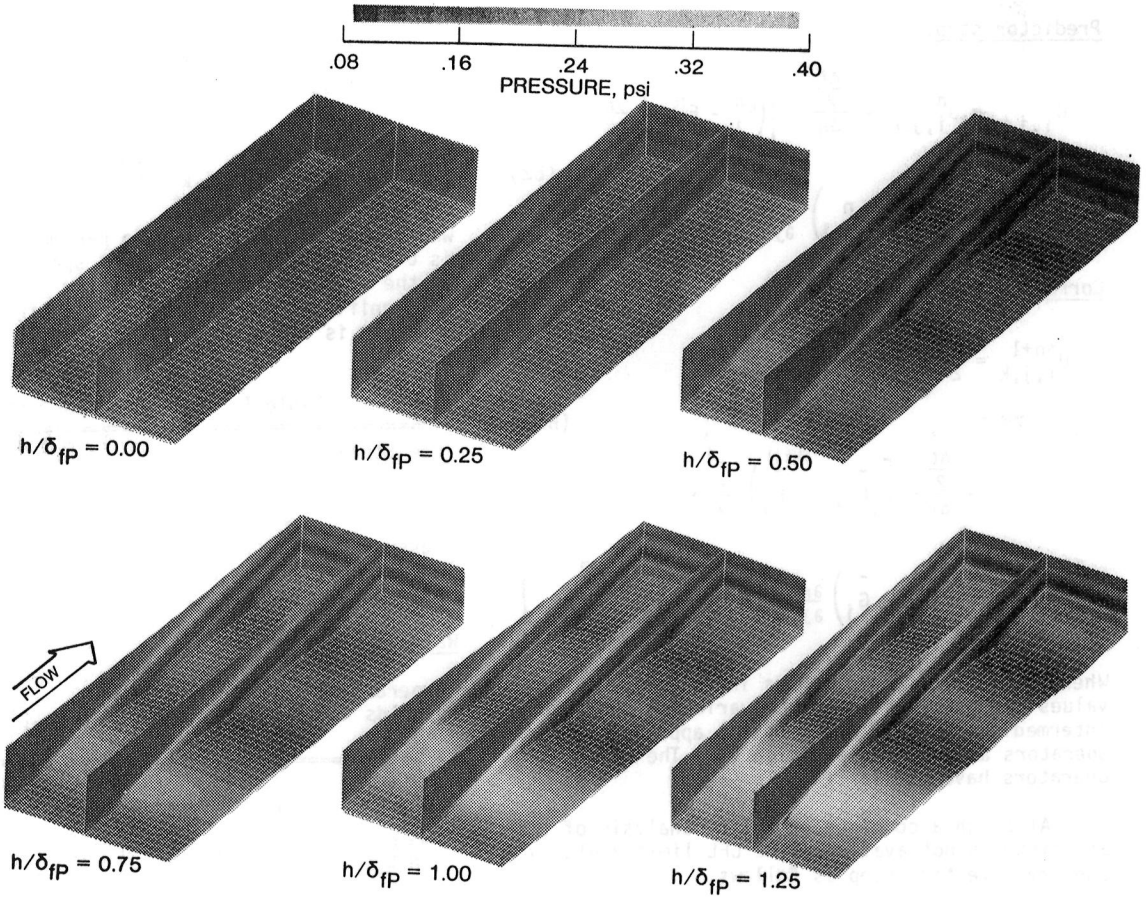


(a) Pressure distributions

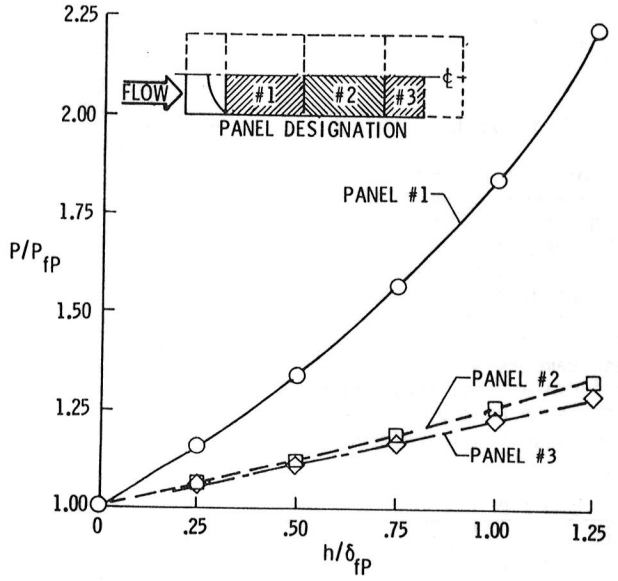


(b) Peak panel pressure.

Fig. 2 Pressure on a quilted panel array with longitudinally aligned flow as a function of bowed height.

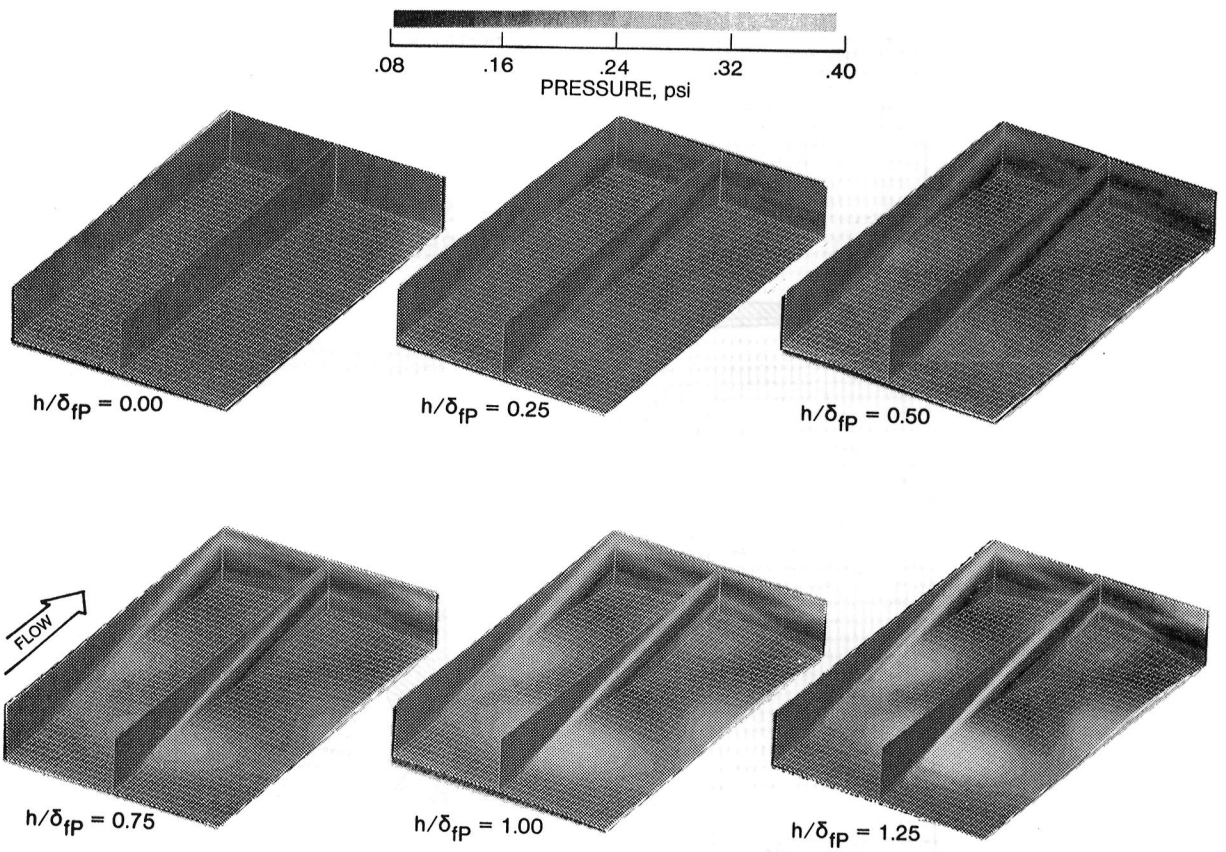


(a) Pressure distributions.

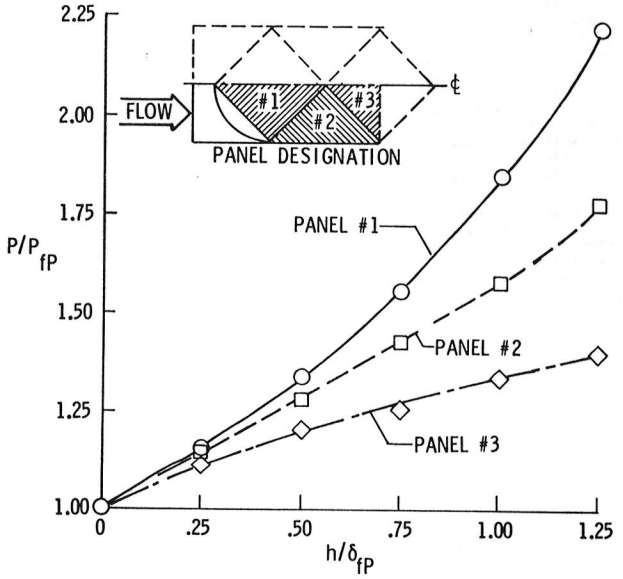


(b) Peak panel pressure.

Fig. 3 Pressure on a quilted panel array with diagonally aligned flow as a funtion of bowed height.

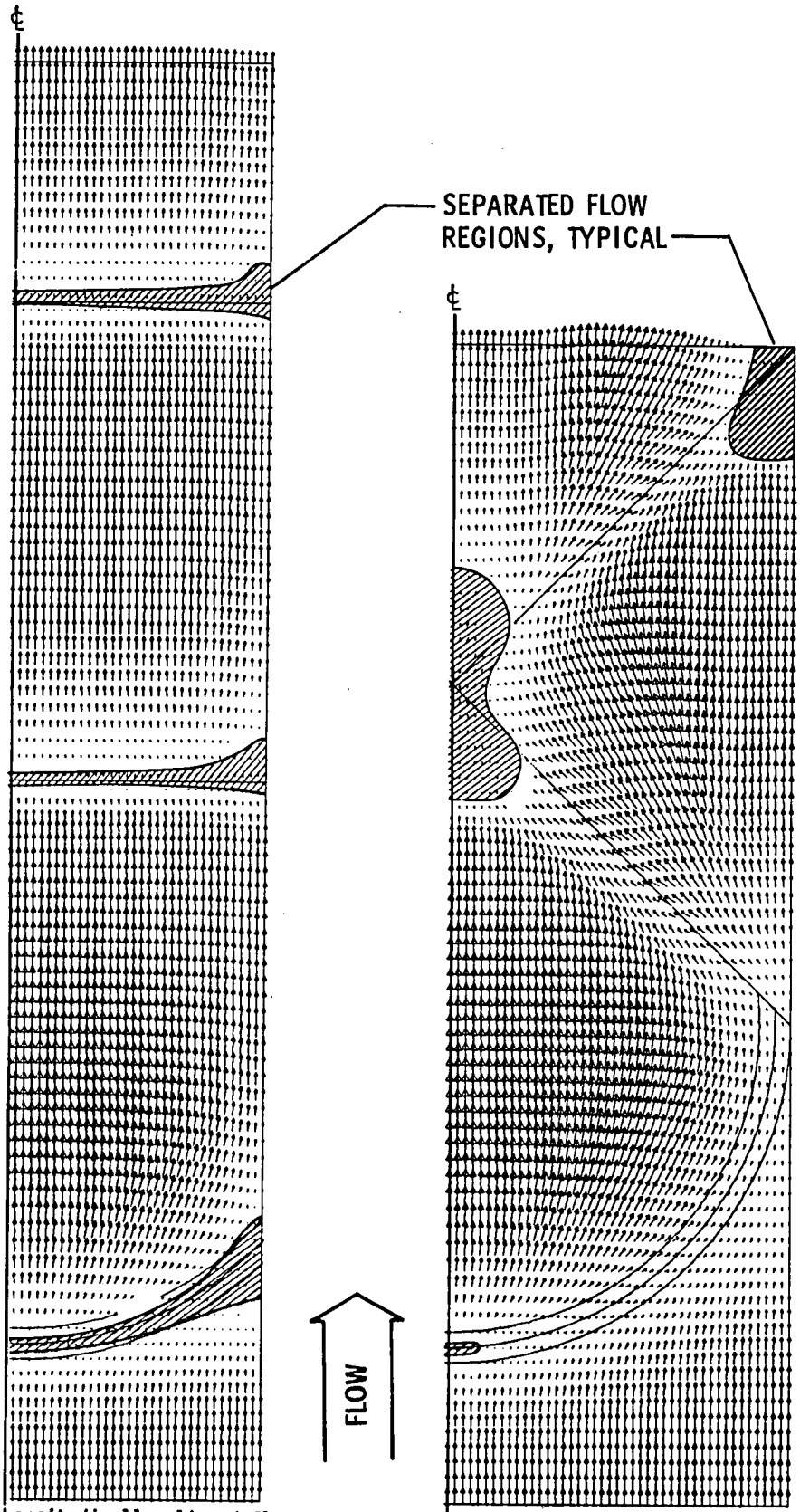


(a) Longitudinally aligned flow.

(b) Diagonally aligned flow.

Fig. 4 Streamwise/crossflow velocity vectors near the surface of quilted panel arrays with bowed height $h/\delta_{fp} = 1.0$.

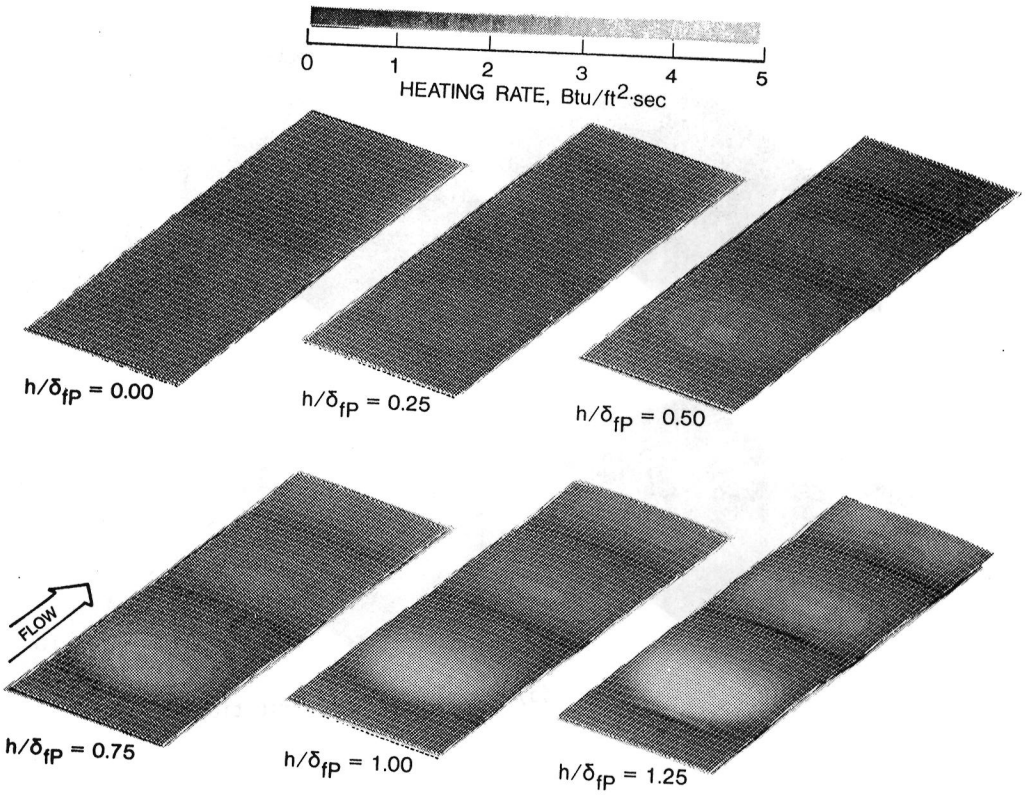


(a) Heating rate distributions.

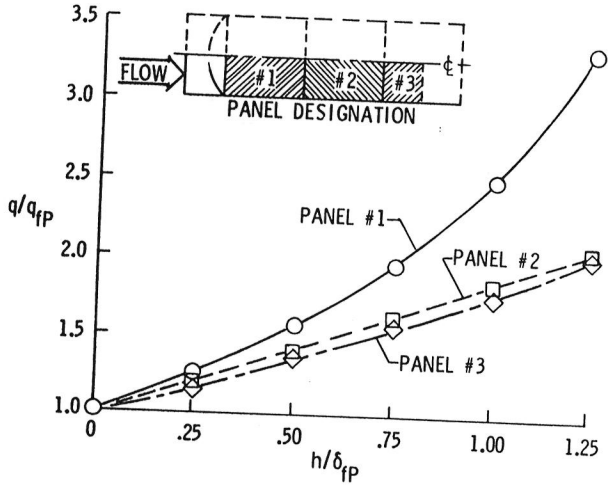


(b) Peak panel heating rate.

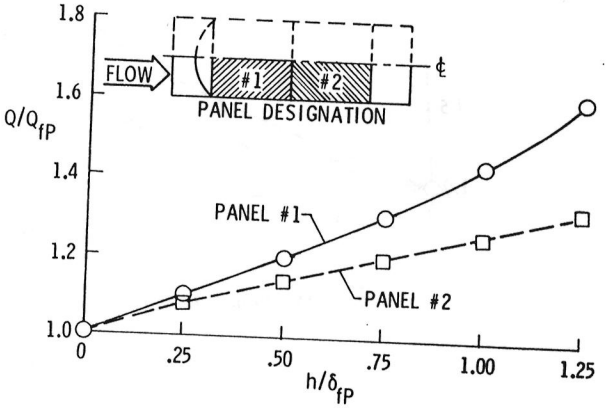


(c) Integrated panel heating load.

Fig. 5 Heating on a quilted panel array with longitudinally aligned flow as a function of bowed height.

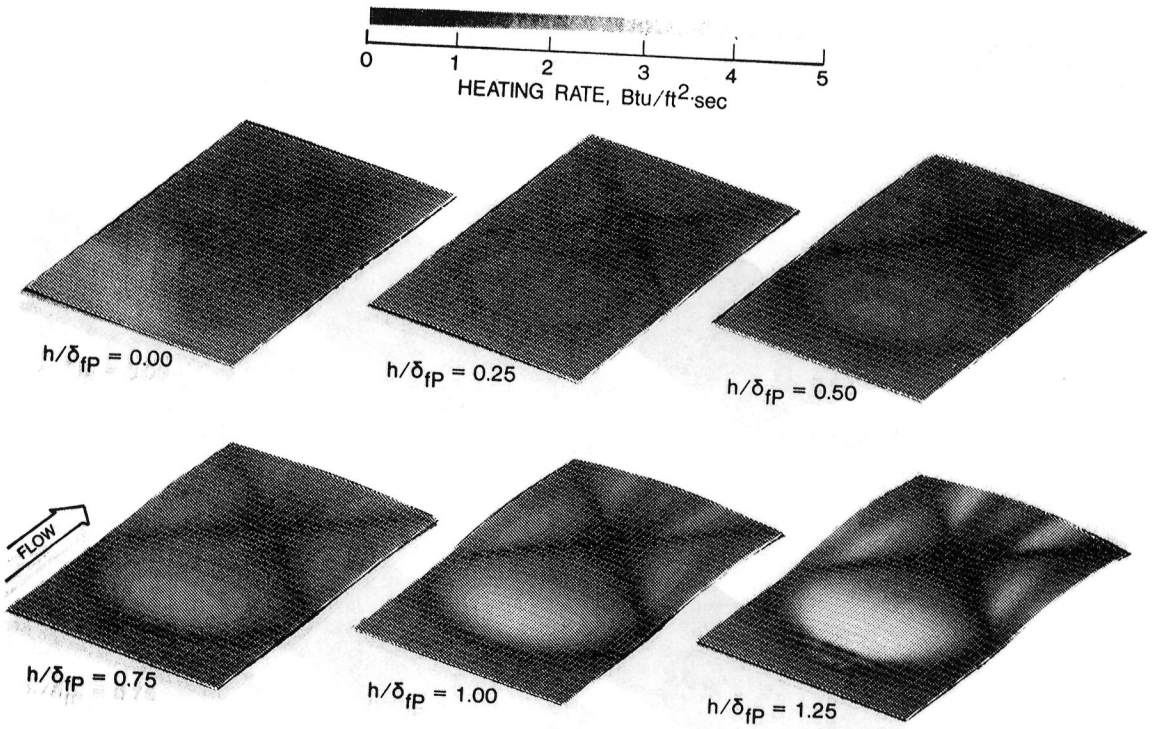


(a) Heating rate distributions.

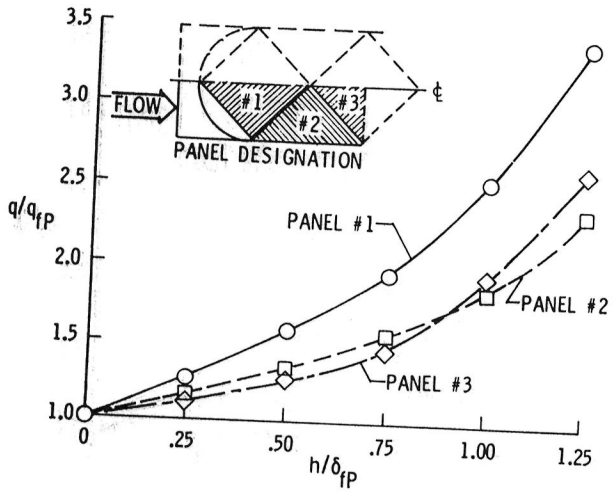


(b) Peak panel heating rate.

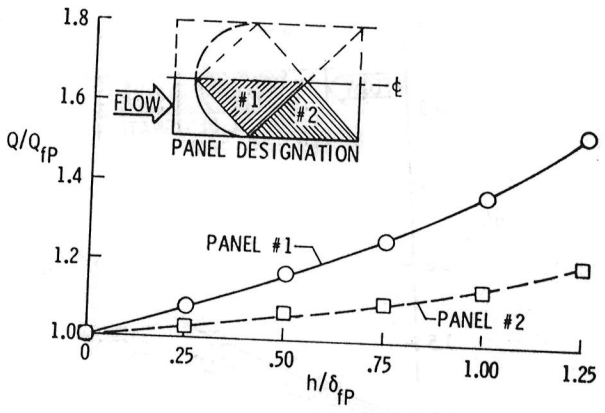


(c) Integrated panel heating load.

Fig. 6 Heating on a quilted panel array with diagonally aligned flow as a function of bowed height.

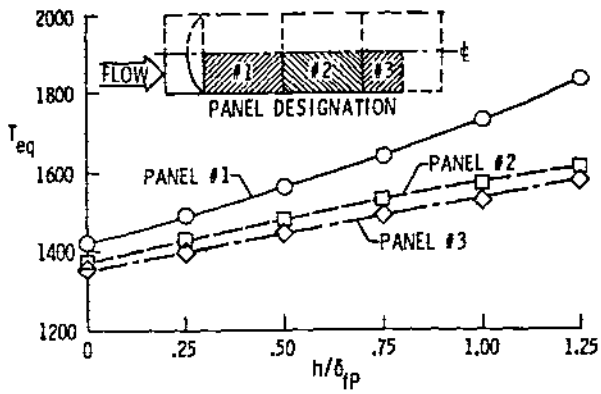


(a) Longitudinally aligned flow.

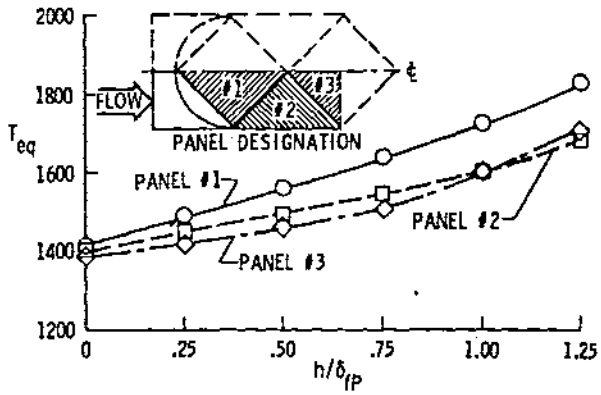


(b) Diagonally aligned flow.

Fig. 7 Maximum equivalent wall radiation equilibrium temperature as a function of bowed height.

| 1. Report No. | 2. Government Accession No. | 3. Recipient's Catalog No. |
|---|---|---|
| NASA TM-86280 | | |

| 4. Title and Subtitle | 5. Report Date |
|---|---|
| Aerothermal Loads Analysis for High Speed Flow Over A Quilted Surface Configuration | August 1984 |
| | 6. Performing Organization Code: 506-53-53-05 |
| 7. Author(s): George C. Olsen and Robert E. Smith | 8. Performing Organization Report No. |
| | 10. Work Unit No. |
| 9. Performing Organization Name and Address: NASA Langley Research Center, Hampton, VA 23665 | 11. Contract or Grant No. |
| | 13. Type of Report and Period Covered: Technical Memorandum |
| 12. Sponsoring Agency Name and Address: National Aeronautics and Space Administration, Washington, DC 20546 | 14. Sponsoring Agency Code |

15. Supplementary Notes

This paper was presented at the AIAA 17th Fluid Dynamics, Plasma Dynamics and Lasers Conference, June 25-27, 1984, Snowmass, Colorado, AIAA Paper No. 84-1630

16. Abstract

Hypersonic laminar flow over a quilted surface configuration was investigated to determine the pressure and heating loads to the surface. The quilted surface configuration simulates an array of metallic Thermal Protection System panels that are bowed in a spherical shape as a result of thermal gradients through the panel thickness. Panel "bowed heights" (deflection of panel from its original flat configuration) from zero to 1.25 times the local boundary layer thickness were investigated for flows both longitudinally and diagonally aligned with the panels. The flow field over the configuration was mathematically modelled using the time-dependent three-dimensional conservation of mass, momentum (Navier-Stokes), and energy equations. A boundary mapping technique was used to obtain a rectangular parallelpiped computational domain, and a MacCormack explicit time-split predictor-corrector finite difference algorithm was used to obtain steady-state solutions. Results show that for bowed heights less than or equal to the local boundary layer thickness total integrated heating loads vary linearly with bowed height. The total integrated heating load on the leading panel increase to less than 1.44 and 1.26 times the flat plate value, respectively. When the bowed height exceeds the flat plate boundary layer thickness heating rates increase more rapidly, vorticity effects become significant and flow beings to separate ahead of the leading panel.

| 17. Key Words (Suggested by Author(s)) | | 18. Distribution Statement |
|---|---|---|
| Aerothermal Loads | 3-D Wavy Surface | UNCLASSIFIED - UNLIMITED |
| Navier-Stokes | Viscous Interacting Flow | SUBJECT CATEGORY 34 |
| Metallic TPS | | |

| 19. Security Classif. (of this report) | 20. Security Classif. (of this page) | 21. No. of Pages | 22. Price |
|---|---|---|---|
| UNCLASSIFIED | UNCLASSIFIED | 14 | A02 |